THE ASTROPHYSICAL JOURNAL, 283:731–744, 1984 August 15

HIGH-RESOLUTION, FAR-ULTRAVIOLET STUDY OF BETA DRACONIS (G2 Ib–II): TRANSITION REGION STRUCTURE AND ENERGY BALANCE[1]

A. BROWN[2]
Department of Physics, Queen Mary College, London, and
Joint Institute for Laboratory Astrophysics, University of Colorado and National Bureau of Standards

C. JORDAN[2]
Department of Theoretical Physics, University of Oxford

R. E. STENCEL[2] AND J. L. LINSKY[2,3]
Joint Institute for Laboratory Astrophysics, University of Colorado and National Bureau of Standards

AND

T. R. AYRES
Laboratory for Atmospheric and Space Physics, University of Colorado
Received 1982 March 30; accepted 1984 January 6

ABSTRACT

High resolution far-ultraviolet spectra of the star β Draconis have been obtained with the *International Ultraviolet Explorer* satellite. The observed emission-line fluxes have been used to derive the mean emission measure distribution, which is used to construct models of the density and temperature variation with height as a function of the transition region pressure. The range of appropriate pressures is investigated from density-sensitive line ratios and through arguments concerning line opacities. The optimum pressure in a spherically symmetric, homogeneous atmosphere is $P_e/k \approx 1 \times 10^{14}$ cm^{-3} K at 2×10^5 K. The X-ray flux measured with the *Einstein Observatory* is discussed in relation to models that extend to coronal temperatures.

The line widths are greater than expected from the appropriate electron temperatures. The profiles of the permitted lines are broader than those of the intersystem lines, indicating broadening through high opacity in addition to nonthermal motions. The enhanced red wings of the optically thick lines show the presence of differential motions in the line-forming region. In principle, these could be due either to an accelerating outflow, a decelerating downflow, or both. The relative wavelengths of the optically thin lines show a small redshift of the lines formed at $\sim 6 \times 10^4$ K with respect to those formed at ~ 8000 K.

The high coronal temperature ($\sim 1.5 \times 10^7$ K) is much greater than that expected from a thermally driven wind. Either this hot plasma is confined by magnetic fields, or if not, then it is heated by some process which is capable of heating plasma to $20 \times T_{esc}$. The X-ray emission cannot originate in a thermally driven wind, and there is no evidence for a wind in either the X-ray or ultraviolet data.

The radiative losses from the chromosphere and transition region are ~ 60 times those of the same solar regions. Because the pressure and temperature gradients are smaller, thermal conduction is not significant. The relatively low X-ray emission measure compared with the solar atmosphere is consistent with this difference in the energy balance. It is shown that simple acoustic waves cannot carry a flux to match the radiation losses. Other forms of energy transport by waves cannot be excluded. The energy redistributed in the turbulent motions is comparable with the observed energy losses.

Subject headings: stars: chromospheres — stars: coronae — stars: individual — stars: late-type — stars: supergiants — ultraviolet: spectra

I. INTRODUCTION

The region of the H-R diagram occupied by the G supergiants and bright giants is of great interest in the study of chromospheric structure and evolution. Two major patterns of chromospheric behavior are present; some stars, like β Dra (G2 Ib–II), show evidence for hot chromospheres, transition regions, and coronae, while others, for instance ϵ Gem (G8 Ib), show only a cool chromosphere and a strong cool stellar wind (Linsky and Haisch 1979; see reviews by Dupree 1981 and Linsky 1981). A further group, the "hybrid" stars, exists, the members of which, e.g., β Aqr (G0 Ib) and α Aqr (G2 Ib), show evidence of chromospheres, transition regions, and cool stellar winds but no hot coronae (Hartmann, Dupree, and Raymond 1980, 1981). The change in structure from the presence of 10^6 K plasma to the presence of material no hotter than $\sim 10^4$ K seems to be correlated with the onset of the strong stellar winds (Stencel and Mullan 1980). Since few bright stars, which can be studied at high resolution with *IUE*, exist in the region of the H-R diagram where this change occurs, progress in understanding these phenomena must depend on detailed study of these brightest stars.

We chose β Dra for study with the *International Ultraviolet Explorer* (*IUE*) satellite, since it lies in this interesting region of the H-R diagram near the hybrid stars α and β Aqr. Previous *IUE* observations of β Dra were presented by Basri and Linsky (1979) and Basri, Linsky, and Eriksson (1981), who

[1] Based on observations made on the *International Ultraviolet Explorer* satellite from the NASA/Goddard Space Flight Center and ESA Villafranca Tracking Stations.
[2] Guest Observer, *International Ultraviolet Explorer*.
[3] Staff Member, Quantum Physics Division, National Bureau of Standards.

computed a chromospheric model based on the Mg II and Ca II resonance line profiles. Prompted by these results, we have made observations at high resolution so that line profiles could be included in the modeling of the atmospheric structure and energy balance. A preliminary analysis has been reported (Brown *et al.* 1982).

In § II we present our *IUE* observations of β Dra and data on the emission lines seen in these spectra. In § III the interpretation of the emission-line widths and shifts is discussed and implications are drawn in terms of atmospheric properties. The emission measure distribution is derived in § IV, and density diagnostics involving both line ratios and line opacity arguments are investigated. The methods for calculating spherically symmetric models of the atmospheric structure are outlined in § V, and several such models are presented. The extension of these models to $\log T_e > 5.3$ using the observed X-ray flux is also discussed. In § VI the energy balance of our "optimum" model is investigated, and possible modes of energy transport and deposition are discussed. Finally, our conclusions are presented in § VII.

II. IUE OBSERVATIONS

a) *IUE Spectra and Data Reduction*

We obtained a high dispersion *IUE* spectrum of β Dra in the 1150–2000 Å region with a 1273 minute exposure on 1981 October 19 (image SWP 15293).[4] At the same epoch a low dispersion SWP spectrum and several high dispersion exposures of the Mg II λ2800 region were obtained. These data have been augmented by earlier spectra from collaborative programs and the data archives. Information concerning all the spectra used in this study is given in Table 1.

The new *IUE* data were all processed at the GSFC *IUE* ground station, and the spectra were extracted using the standard IUESIPS software (Turnrose and Harvel 1982). Analysis of the spectra was performed using the standard procedures at the Boulder *IUE* Regional Data Analysis Facility. For high resolution data the interorder background was smoothed by a median filter followed by a double-pass running mean before subtraction from the stellar spectrum. The optimum order-dependent echelle blaze correlation described by Ake (1981) was used to obtain the ripple-corrected net spectrum. The flux calibrations of Bohlin and Holm (1981) and Cassatella, Ponz, and Selvelli (1981) were used for the low and high resolution spectra, respectively. The "emission line" version of the Cassatella, Ponz, and Selvelli values was used.

[4] This collaborative NASA and SERC observation is the longest continuous *IUE* exposure to date and was achieved by combining three consecutive observing shifts during a period of exceptionally low particle background radiation.

b) *Line Identifications*

The low resolution, short-wavelength spectrum of β Dra is shown in Figure 1 and displays emission lines formed in a range of excitation conditions between 7000 K (O I) and 2×10^5 K (N V). Resonance lines of O I, Si II, Si IV, C II, C IV, and N V are seen, along with intercombination lines of C I, O I, O III, Si III, C III, and N III. The stellar photospheric continuum rises steeply longward of 1700 Å. High dispersion emission line profiles from our long SWP exposure are presented in Figure 2. The lines seen in Figures 1 and 2 can be identified through previous experience with solar and stellar UV spectra. The high resolution spectrum provides confirmation of the importance of fluorescent excitation of S I (UV9) by O I (Brown and Jordan 1980) since other potentially strong S I lines (e.g., UV2) are absent or very weak.

Two features, blended at low resolution but resolved in the high resolution spectra, deserve comment. The first is a narrow line at 1351.6 Å, which is also seen in the solar spectrum. Although Jordan (1965) pointed out that this wavelength fits a line of Cl I (UV2), this identification became unsatisfactory when improved spectra failed to show other members of the multiplet. However, Shine (1983) showed that another member of the multiplet (1335.7 Å) with the same upper level ($4s\ ^2P_{1/2}$) might be pumped by the C II λ1335.66 + λ1335.71 blend. This suggestion is appealing since the λ1351.6 line does *not* appear in cooler stars where C II is absent. Solar spectra obtained with the NRL HRTS instrument (see illustration in Jordan *et al.* 1978) show that the line behaves from center to limb in the same way, as do other nearby lines of neutral species. While the line seems that of a neutral species, the identification with the Cl I λ1351.6 line is presently still in doubt.

The other feature extends between 1309 and 1310 Å, and appears to be a blend of broad and narrow lines at 1309.5 ($\pm$0.25) and 1309.9 ($\pm$0.1) Å. There is no entirely satisfactory

TABLE 1

IUE OBSERVATIONS OF β DRACONIS

Image Number[a]	Dispersion	Date	Exposure Time (minutes)	THDA[b]
LWR 4700	high	1979 Jun 5	8	14°.5
LWR 7566	high	1980 Apr 20	8	13.2
LWR 10655	high	1981 May 19	10	14.5
LWR 11806	high	1981 Oct 19	8	12.8
LWR 11807	high	1981 Oct 19	8	13.2
LWR 11808	high	1981 Oct 20	8	13.8
SWP 2348	low	1978 Aug 21	24	...
SWP 2349	low	1978 Aug 21	60	...
SWP 2350	low	1978 Aug 21	10	...
SWP 5437	high	1979 Jun 4	360	...
SWP 15292	low	1981 Oct 19	30	...
SWP 15293	high	1981 Oct 19	1273	...

[a] The spectral ranges of the cameras are 2000–3000 Å (LWR) and 1150–2000 Å (SWP).

[b] Nominal sensitivity of LWR camera adjusted by -1.1% per THDA degree below 14°.5.

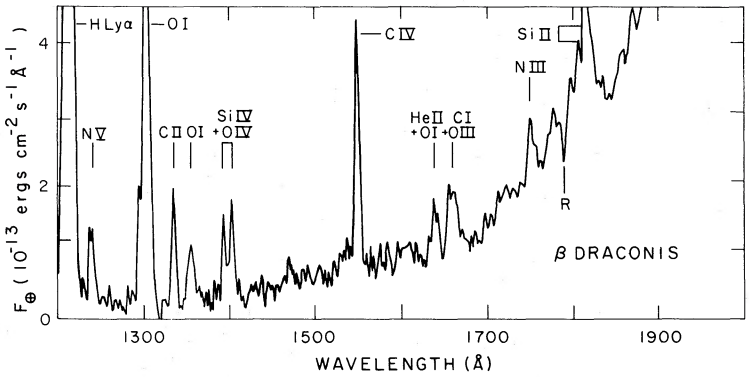

FIG. 1.—Low resolution, short wavelength *IUE* spectrum of β Dra obtained from image SWP 15292 (30 minute exposure). Observed monochromatic flux is plotted as the ordinate. Prominent emission lines are identified. Those portions of the spectrum above the upper limit of the diagram are overexposed. "R" denotes positions where reseaux marks affect the spectrum.

identification for this feature, but the correlation of its strength and overall width with the nearby O I lines suggests a photoexcitation process. Si II (UV3) has components at 1309.27 and 1304.37 Å. Emission from the 1304.37 Å line, distorted by interstellar absorption, could be present, with the red wing overlapping the O I λ1304.86 line. Thus, Si II at 1309.27 Å could account for the line at 1309.5 Å. P II (UV2) has components from $J = 1$ at 1309.88, 1304.69, and 1301.88 Å. It could account for the 1309.9 Å feature, but the narrow width of the observed line and low abundance of phosphorous cast doubt on the suggestion. Underhill (1981) has suggested that dielectronic recombination may cause emission in Si II (UV13.04) which has upper level components ($^2F^o_{5/2,7/2}$) below and above the ionization limit. However, the lines at 1309.46 and 1309.77 Å are from the upper level $^2F^o_{5/2}$ for which there is no route for pumping with the O I lines. In other cool stars the feature is present when C II is absent, and it does not obviously correlate with the Si II λλ1808, 1817 lines. However, neither is it always

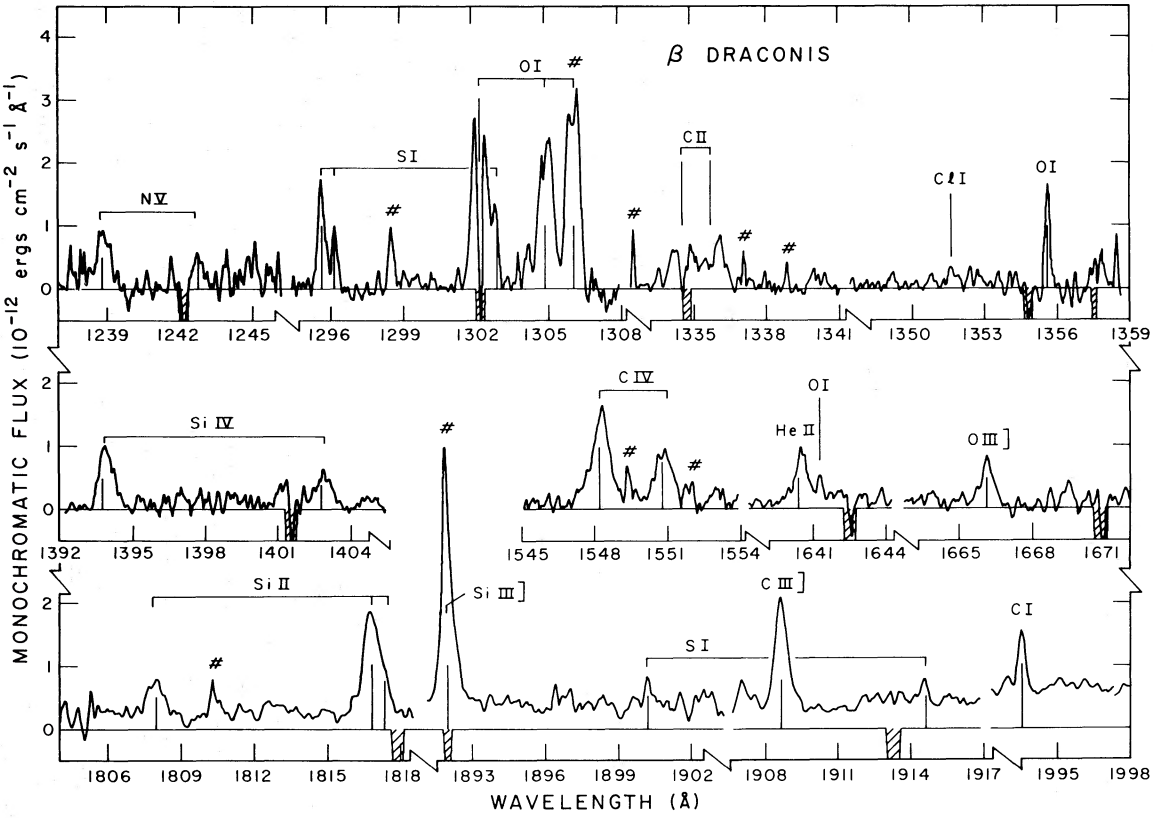

FIG. 2.—Selected high resolution emission line profiles of β Dra. Ordinate is the observed monochromatic flux, and abscissa is a wavelength scale relative to the flux-weighted mean velocity of narrow chromospheric emission lines (see text). The spectrum shortward of 1800 Å is from image SWP 15293, while that longward of 1800 Å is from SWP 5437. The spectra were smoothed with a three-point running mean before plotting. The rest wavelengths of prominent emission lines are shown by vertical tick marks. Cross-hatched dropouts below the spectrum refer to regions affected by reseaux or saturation. Strong particle radiation noise spots are indicated by "#" symbols.

present when the S I lines pumped by O I are strong. For these various reasons we are not satisfied that the feature is yet correctly identified.

c) *Line Fluxes, Widths, and Positions*

The emission-line fluxes derived from the available spectra of β Dra are presented in Table 2, along with values for the line centroid velocity, V_L, and the full width at half-maximum. The wavelengths given are from Kelly and Palumbo (1973). A Gaussian line-fitting routine, previously discussed by Ayres *et al.* (1982), was used to derive the integrated fluxes, velocities, and widths for the strongest emission lines. The fitting is performed on the upper half of the line, where the signal-to-noise is best, and therefore, the line centroid velocity represents the position of this portion of the line. Velocities were determined after smoothing by a three-point running mean, while the widths were obtained from the unsmoothed profile. The flux-weighted mean of the observed positions for the neutral optically thin lines of O I (1356 Å), S I (1295, 1296, 1303, and 1915 Å), Cl I (1352 Å), and C I (1994 Å) was used to define a zero velocity since no arc lamp calibration spectrum was taken. Figure 3 illustrates the quality of the Gaussian fitting for the well-exposed C IV resonance lines.

Longward of 1800 Å, values from the earlier high resolution exposure (SWP 5437; Ayres *et al.* 1982) have been used because our longer exposure is saturated in this region. For very weak lines and lines with strong central self-reversals, such as the O I resonance triplet, high resolution fluxes were obtained by direct integration of the spectrum. Low resolution fluxes from images SWP 2348 – 50 (Basri, Linsky, and Eriksson 1981) and from our low resolution image are given for comparison. No corrections for interstellar absorption have been made to the values in Table 2. Good agreement is seen between the low dispersion fluxes for strong emission lines and continuum regions, even though the spectra were obtained 3 yr apart. Thus, there is no evidence from these data for significant variability in the chromospheric and transition region emission.

III. INTERPRETATION OF LINE WIDTHS AND TRANSITION REGION VELOCITIES

The displacements of the line centroids from rest wavelength and the line widths (FWHM) uncorrected for instrumental broadening were given in Table 2. The instrumental resolution is 30 km s^{-1}, corresponding to 0.15 Å at 1500 Å, and the widths were corrected for this effect by adopting Gaussian profiles. This correction is significant only for narrow lines of neutral species. The line shifts and corrected widths expressed as velocities are plotted against temperature in Figure 4.

Several systematic effects can be seen in Figure 4. First, the widths of intersystem lines are much smaller than those of permitted lines formed at comparable temperatures. This excess width can be attributed to opacity broadening in the

TABLE 2

FAR-ULTRAVIOLET LINE FLUXES, WIDTHS, AND SHIFTS

Multiplet	λ (Å)	Line Flux (10^{-13} ergs cm^{-2} s^{-1} Å^{-1}) 15293(H)[a]	5437(H)[a]	2348–50(L)[a]	15292(L)[a]	v_L (km s^{-1})	FWHM (Å)
C III (4)	1176.	...	...	7.5:	...	...	...
Si III (2)	1206.5	4:[b]	...	...	...	...	...
N V (1)	1238.8	3	...	7.8	7.5	+19	0.55
	1242.8	2	...			+4	0.53
S I (9)	1295.7	4	...	...	...	+4	0.32
	1296.2	2	...	...	...	+11	0.40
	1302.9	2:	...	...	...	−10:	0.33:
O I (2)	1302.2	>9[b]	...			+16	0.71
	1304.9	13[b]	11	64	74	+20	0.58
	1306.0	20[b]	14			+12	0.50
Si II?	1309	3[b]	...	...	...	...	...
C II (1)	1334.5	>2[b]	...	9.5	10.3	+13	0.80
	1335.7	7[b]	...			+21	0.86
Cl I (1)	1351.7	1	...	...	...	+3	0.38
O I (1)	1355.6	3	...	7.5	10:	+4	0.19
Si IV (1)	1393.6	6	5	7.5	19:	+38	0.72
	1402.8	4	...	8.1		+44	0.87
O IV	1401	2	...	...	...	...	...
Si II	1526	2	...	...	...	...	...
C IV (1)	1548.2	13	11	24	21	+26	0.81
	1550.8	9	8			+26	1.00
He II (12)	1640.4	6	5	4.8	8:	+35	0.61
O I	1641.3	2	...			+1	0.25
C I (2)	1657 bl	9[b]	...	8.5	14.4	...	...
[O III]	1660.8	2[b]	...	5.4	...	...	...
	1666.2	3	...			+6	0.55
Si II (1)	1808.0	S[c]	3	8.3	(S)	+18	0.61
	1816.9 bl	S	(S)	27.		+1	0.69
Si III] (1)	1892.0	S	13	17.	15.	+12 ± 5	0.66
C III] (0.01)	1908.7	S	7	11.	6.9	+2 ± 5	0.55
S I	1914.7	S	1	...	...	−5 ± 4	0.08
C I (32)	1993.6	S	4	...	...	+1 ± 5	0.28

[a] SWP image number. H = high dispersion, L = low dispersion.

[b] These line fluxes were obtained by direct integration of the data rather than by fitting of a Gaussian profile.

[c] Saturated line.

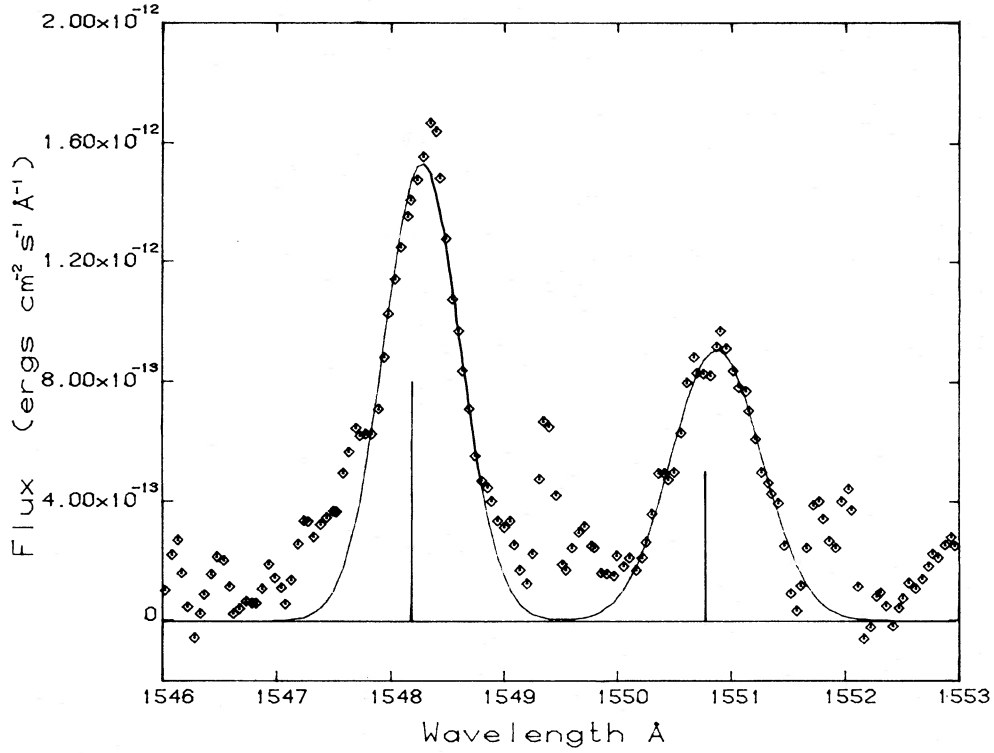

FIG. 3.—Least-squares Gaussian fitting (*solid curve*) for the C IV resonance line profiles (*symbols*) from Fig. 2. Vertical lines indicate the rest wavelength of the C IV lines in the velocity system defined by the narrow chromospheric lines. Note the asymmetry present in the line profiles.

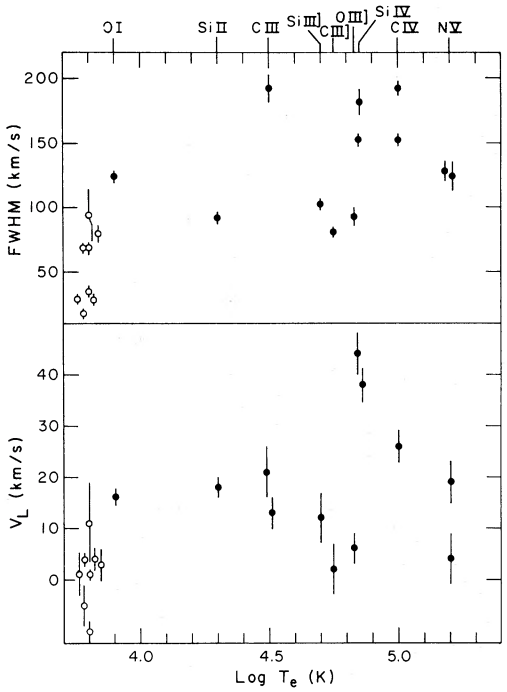

FIG. 4.—Variation of line centroid velocity, v_L, and full width at half-maximum, FWHM, as a function of temperature. Temperatures adopted are those at which the $g(T)$ function (see eq. [2]) has its maximum value, except for O I, for which an estimate of the optimum region of line formation is used. The line centroid velocity zero point is defined by the flux-weighted mean velocity of narrow chromospheric emission lines (see text). Ions used are indicated at the top of the figure. Solid symbols indicate lines formed in the upper chromosphere and transition region, while open symbols represent the narrow chromospheric emission lines. Error bars shown represent ±1 standard deviation (1 σ).

resonance lines (e.g., C II, Si IV, and C IV). Further evidence that these lines are at least marginally optically thick is provided by the ratios of the peak fluxes within each multiplet which are all less than their optically thin values of 2:1. The resonance lines of N V seem to be optically thin on the basis of their line widths. Since the intersystem lines are certainly optically thin, their widths allow the effects of nonthermal mass motions to be estimated. Second, the intersystem lines formed at $T_e \approx 5\text{–}7 \times 10^4$ K are displaced by $+8 \pm 4$ km s^{-1} compared with neutral optically thin chromospheric lines chosen to define the zero velocity. This shift is small and will require confirmation by future higher quality measurements before any major conclusions are drawn from it. However, other lines which are optically thin, such as the Si II λ1808, He II λ1640, and N V λ1238 lines, also show redward displacements. At face value these shifts indicate a new excess of emission from downward-moving material over that from material moving upward. Similar results for a number of stars are presented by Ayres *et al.* (1983). The redward asymmetries of the optically thick resonance lines can be explained by line formation in a turbulent medium with a combination of accelerating upflows and decelerating downflows. Calculations appropriate to these conditions were presented by Hummer and Rybicki (1968). Athay (1972) and Basri (1980) have also considered the combined effects of opacity and turbulence, the latter in the context of the Mg II and Ca II resonance lines. Basri, Linsky, and Eriksson (1981) discussed the asymmetry of the Ca II K and Mg II *k* lines in β Dra and suggested that small-scale circulation motions were required to account for these profiles, since a simple flux-conserving vertical flow could not fit both lines. Our results are in agreement with this suggestion. We are unable to reconcile the observations of both the optically thin and thick lines with formation in an outflow leading to a wind.

Results somewhat similar to those derived from the optically thin lines have been found in the Sun. Net downflows of between 5 and 20 km s^{-1} have been seen in transition region lines, both in spatially resolved observations of plages and the supergranulation network (Doschek, Feldman, and Bohlin 1976; Feldman, Cohen, and Doschek 1982) and from spatially averaged quiet-Sun spectra (Roussel-Dupré and Shine 1982). In the solar case all the lines concerned, including the resonance lines, are optically thin. Dere (1982) showed that in the Sun the maximum downflow velocity occurs at a temperature near 10^5 K (for a review see, e.g., Brueckner 1981).

The width of the He II λ1640 Baα blend can be used to investigate the temperature at which these lines are formed. The temperature at which the He II lines can be formed can be investigated by computing the line fluxes as a function of temperature. Such calculations show that the temperature would range from $\lesssim 2.5 \times 10^4$ K, if recombination is the dominant process populating the $n = 3$ levels, to $\sim 8 \times 10^4$ K, if collisional excitation in He II Lyβ followed by decay in He II Baα predominates. In the solar atmosphere both processes, plus transfer of photons from Lyβ to Baα through the optically thick Lyβ line, are important. The mean wavelength of the seven components is 1640.43 Å, and the separation of the two strongest components is 0.13 Å. Removing this from the observed total FWHM gives 0.48 Å for the intrinsic width, which by a simple interpolation between low and high temperature intersystem lines (see Fig. 4) implies a temperature of $\sim 3.5 \times 10^4$ K. Therefore, recombination is making some contribution to the He II flux. Hartmann, Dupree, and Raymond (1980) suggested that if recombination dominates a scaling law such that F(X-rays)/F(He II λ1640) $\approx$ 50 should hold. While this may or may not be correct for solar-type main-sequence stars (see Seely and Feldman 1984), in lower gravity stars, including β Dra, too much X-ray flux is predicted.

IV. EMISSION MEASURE DISTRIBUTION AND DENSITY DIAGNOSTICS

a) Emission Measures

Methods for analyzing the fluxes of effectively thin emission lines are well established from solar work (Pottasch 1964; Jordan and Wilson 1971) and are only outlined briefly here. Applications to stellar chromospheres and coronae have been discussed by Jordan and Brown (1981) and applied by Brown and Jordan (1981) to α CMi.

The total surface flux in a collisionally excited, effectively thin emission line can be expressed as

$$F_* = \frac{hc}{\lambda}\frac{1}{2}(0.80)(8.6 \times 10^{-6})\frac{\Omega_{12}}{\omega_1}\frac{N_E}{N_H}\frac{N_1}{N_{ion}}\int_{\Delta h} N_e^2 g(T)dh\,, \quad (1)$$

using a two-level system here for illustration. Here Ω_{12} is the collision strength (Seaton 1962), ω_1 is the statistical weight of the lower level, N_E/N_H is the element abundance, and N_1/N_{ion} is the population of the lower level (=1 in a two-level case). The function $g(T)$ contains the explicit temperature-dependent quantities and is

$$g(T) = T_e^{-1/2}\exp\left(-\frac{W_{12}}{kT_e}\right)\frac{N_{ion}}{N_E}\,. \quad (2)$$

The factor $\frac{1}{2}$ allows for emission both inward and outward from the atmosphere, while the factor of 0.80 is from the approximation $N_H = 0.8N_e$, which assumes hydrogen is predominantly ionized. The quantity W_{12} is the excitation energy. In the region below 2×10^4 K the quantity best considered is $\int N_e N_H dh$, since this eliminates the need to know the detailed behavior of the N_H/N_e ratio. In practice, a multilevel atom is used as necessary, and the total effective excitation rate to a level found. During this process, the sensitivity to N_e and T_e is also investigated. A general review of the spectra of astrophysical plasmas is given by Gabriel and Jordan (1972). We assume initially that the surface area of the emission is that of the stellar photosphere. Models computed using the measured electron density show that this assumption is self-consistent for lines formed at up to 2×10^5 K (see below and Fig. 6). Although atmospheric inhomogeneities (e.g., associated with supergranulation structure or the magnetic field configuration) could exist, it is possible to detect their effects by comparing the density measured from line ratios with that estimated by comparing the opacity and emission measure (see below). This comparison shows that any such effects do not have a significant effect on the average model we calculate.

The observed emission-line fluxes were corrected for interstellar absorption by dust using the mean reddening curve of Savage and Mathis (1979) and a visual absorption, A_V, of 0.3 mag (Breakiron and Upgren 1979). These corrected fluxes were then converted to stellar surface fluxes using an apparent stellar diameter of 3.25 milliarcseconds (mas) derived from the Barnes-Evans relation (Barnes, Evans, and Moffett 1978). The appropriate conversion factor is 1.6×10^{16}.

It has been usual to replace $g(T)$ by a mean value, either some fixed fraction of its peak value (e.g., Pottasch 1964) or an average over a fixed range of $\Delta \log T_e$ (Jordan and Wilson 1971). The stellar spectra available do not allow as large a range of lines to be observed as do solar spectra, and thus the mean emission measure, $\int_R N_e^2 dh$ (R referring to a region $\Delta \log T = 0.30$), is not very well defined between 10^4 and 3×10^4 K. We therefore adopt an alternative approach in which the value of $\int_{\Delta h} N_e^2 dh$ is computed as a function of T_e as if *all* the line were formed at each temperature in turn. Therefore, this emission measure, $E_m(T_e)$ is equivalent to 0.7 $\times E_m(0.3)$, where $E_m(0.3)$ is the quantity used previously. The loci of these solutions are shown in Figure 5, and Table 3 contains the adopted atomic data and derived emission measures from both low and high dispersion fluxes. The value of T_m in Table 3 refers to the peak of the $g(T)$ function, even in cases where the emission measure rises rapidly with decreasing temperature.

Generally, the atomic data adopted, including the ion balance populations, are as discussed by Brown and Jordan (1981), with the following exceptions and additions. The abundances of C, N, O, Si, and Mg have been taken from Luck (1977, 1978) and Luck and Lambert (1981). The main differences between these and solar values are a higher nitrogen abundance and lower carbon and oxygen abundances.

The population calculations including charge transfer for Si ions by Baliunas and Butler (1980) have been examined. The only significant differences from the earlier results of Jordan (1969*a*) arise in regions which contribute little to the total flux. However, for Si II above $\sim 2.5 \times 10^4$ K and Si III below 4×10^4 K the Baliunas and Butler values are used. The collision strength for the $3s^2 3p\ ^2P$–$3s\ 3p^2\ ^2D$ transition in Si II is not yet well determined, and the values given in Table 3 are those suggested by Tully (private communication). The emission measure for this transition is larger than that derived from the upper limit to the flux in the ^2P–^2S multiplet at 1526 Å. Jordan (1969*b*) suggested that in the Sun the ^2D term may be

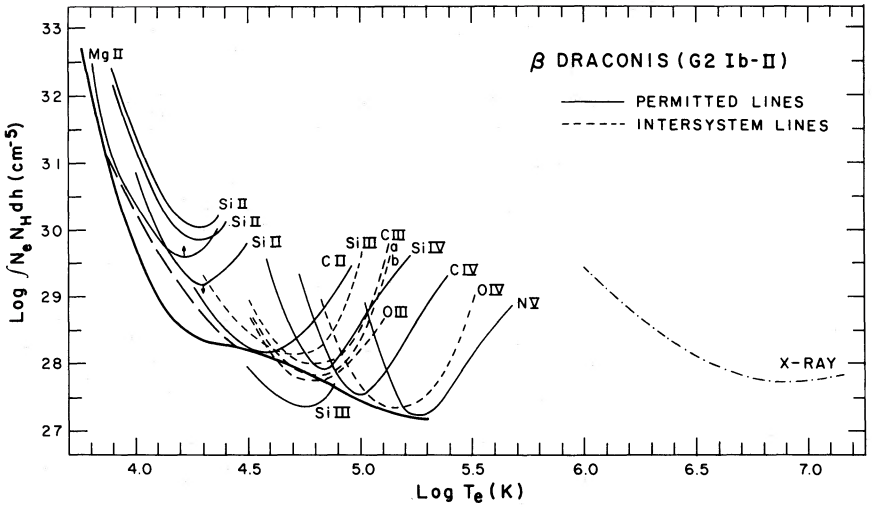

FIG. 5.—Mean emission measure distribution of β Dra (*thick solid line*). Quantity $\int N_e N_H dh$ is used as the ordinate rather than the conventional $\int N_e^2 dh$ (see text). The emission measure loci derived from individual UV emission lines and from the *Einstein* X-ray flux are shown as parabolic-like curves, with minima corresponding to the temperature of maximum ion abundance, T_m. Permitted and intersystem lines are shown as full and dashed curves, respectively. Two loci are shown for C III] appropriate to densities of (*a*) 10^{10} cm^{-3} and (*b*) 10^9 cm^{-3}. Alternative mean emission measure distribution discussed in the text is shown as a thick broken line.

excited mainly from the metastable ^4P levels. Recent calculations of the ^2P–^4P and ^4P–^2D collision strengths by Kingston *et al.* (1983) show that, at the density appropriate to β Dra ($N_e \approx 10^{10}$ cm^{-3} at 10^4 K; see § IV*a*), the contribution from this excitation route should decrease the derived emission measure by a factor of 1.6, bringing the values for the two multiplets into reasonable agreement at 10^4 K. The emission measures given in Table 3 and Figure 5 for the ^2P–^2D transitions would then be reduced by this factor. The cross section for the Si III λ1892 intersystem line has been revised by Baluja, Burke, and Kingston (1980*a*, 1981), and this has been adopted when considering both the absolute flux and density-sensitive line ratios. The transition probability for this line has been calculated by Laughlin and Victor (1979) and Cowan, Hobbs, and York (1982) and measured by Parkinson *et al.* (1983). A value of 1.61×10^4 s^{-1} is used here.

The collision strength for the O III ^3P–^5S transition has been calculated by Jackson (1973), Doschek *et al.* (1978), and more

TABLE 3

ATOMIC DATA AND DERIVED EMISSION MEASURES

Ion	λ (Å)	$F_{*\,\mathrm{corr}}$ (10^4 ergs cm^{-2} s^{-1})	Ω	$g(T_m)$	N_E/N_H	N_1/N_{ion}	E_m (cm^{-5})	log T_m (K)
N V	1238.8	1.2	7.2	3.1(−4)	2.5(−4)	1.0	1.3(27)	5.2
	1242.8	0.8						
	{1240}	3.0	...	...	...	...	2.0(27)	...
O IV	1401.2	0.5	0.6	9.1(−4)	3.2(−4)	1.0	2.4(27)	5.15
C IV	1548.2	4.1	11.2	6.4(−4)	1.3(−4)	1.0	3.4(27)	5.0
	1550.8	2.9						
	{1549}	7.6	...	...	...	...	3.7(27)	...
N III	1752	≤2.6	0.27	9.1(−4)	2.5(−4)	1.0	≤1.1(28)	4.9
Si IV	1393.6	2.0	16.4	2.2(−4)	4.4(−5)	1.0	8.5(27)	4.85
	1402.8	1.4						
	{1396}	5.6	...	...	...	...	1.5(28)	...
O III]	1660.8	0.7	1.1	9.7(−4)	3.2(−4)	0.64	5.6(27)	4.83
	1666.2	1.0						
	{1664}	1.8	...	...	...	...	6.1(27)	...
C III]	1908.7	2.4	0.95	9.8(−4)	1.3(−4)	0.52[a]	1.1(28)	4.75
		...	...	...	...	0.74[b]	7.4(27)	...
Si III	1206.5	1.6	7.9	3.9(−4)	4.4(−5)	0.85	2.5(27)	4.7
Si III]	1892.0	5.0	3.2	8.5(−4)	...	0.85	1.4(28)	...
C II	1334.5	>1.1	3.0	1.6(−4)	1.3(−4)	1.0	>1.4(28)	4.5
	1335.7	2.6	6.0				1.6(28)	...
	{1335}	3.6	...	...	...	...	1.1(28)	...
Si II	1526	<0.8	1.7	2.9(−5)	4.4(−5)	1.0	<1.6(29)	4.3
	1808	2.7	0.73	6.6(−5)	...	1.0	6.7(29)	...
	{1814}	8.8	4.39	...	...	...	1.1(30)	...
Mg II	2800	2.6(2)	35.4	2.6(−4)	5.9(−5)	1.0	>3.9(29)	4.2

[a] $N_e = 10^{10}$ cm^{-3}.
[b] $N_e = 10^9$ cm^{-3}.

NOTE.—Braces indicate values derived from low resolution *IUE* spectra. When no blending occurs, these values should be more accurate than those derived from high resolution data.

recently by Baluja, Burke, and Kingston (1980*b*), whose value we use. The transition probability has been calculated by Doschek *et al.* (1978). The atomic data adopted for the O IV ^2P–^4P multiplet are those of Hayes (1982). The collision cross section for the N III ^2P–^4P transitions calculated by Nussbaumer and Storey (1979) is used. The data for C III are as given in Table 2 (case 3) of Dupree, Foukal, and Jordan (1976); very similar results were derived by Dufton *et al.* (1978). The collision strength for the C II resonance lines given by Magee *et al.* (1977) is adopted here.

In the first instance the mean emission measure is best defined by the effectively thin lines of C II, C IV, Si IV, and N V. The Mg II lines are here treated as collisionally excited and effectively thin, but they give only a lower limit to the emission measure because substantial interstellar absorption is likely to occur. A reseau affects the high dispersion profile of the C II line terminating on the ground level, but the flux in the lines ending on the excited J state is also available and has been used to derive the locus shown in Figure 5. Since some interstellar absorption may occur for this line, the C II locus should probably be considered as a lower limit. The general agreement between lines of different elements suggests that there are no significant discrepancies in the elemental abundances adopted. In general, for the unblended lines the values of the emission measure determined from *IUE* low resolution fluxes should be more accurate than those from high resolution fluxes, and the former values are primarily used in determining the mean emission measure distribution shown in Figure 5. This mean distribution is chosen to minimize the total radiative losses. An alternative mean distribution is also shown, and the results of adopting this distribution are discussed later.

As can be seen from Figure 5, the main discordant result is the low value of the emission measure derived from the Si III λ1206 resonance line. Also the λ1206/λ1892 flux ratio is lower than in the low density limit, even when the calculations by Nicolas (1977) are corrected for the new cross section for the λ1892 transition. An underestimate of the flux in the λ1206 line would resolve both discrepancies. This could arise through overcorrection for the background at 1206 Å due to the presence of geocoronal H Lyα emission in the adjacent order. Other possible sources of error are uncertainties in the *IUE* calibration below 1225 Å, Si III interstellar absorption, interstellar absorption in the wings of H Lyα, and, least likely, the possibility of unusual interstellar reddening at short wavelengths.

b) Density Diagnostics

The ratios of intersystem transitions to permitted transitions are potentially useful for measuring the electron density. The spectrum of β Dra contains a number of intersystem lines, but a comparison of their ratios shows that they are all in their low density limit to within observational uncertainties.

The ratios C III λ1909/O III λ1666; O III λ1666/Si IV λ1403, and C III λ1909/Si IV λ1403 have been calculated as a function of density by Doschek *et al.* (1978). To use their results the abundances they adopted (Withbroe 1976) must be changed to those in Table 3. These three ratios then yield, $N_e \leq 10^{10}$ cm^{-3}, $N_e \approx 10^{10}(\pm 5 \times 10^9)$ cm^{-3}, and $N_e \approx 3 \times 10^9(\pm 3 \times 10^9)$ cm^{-3}, respectively.

The other intersystem lines observed will also behave in the "coronal" limit. O IV λ1401 is sensitive to N_e only at $N_e \gtrsim 3 \times 10^{10}$ cm^{-3}, N III λ1750 only at $N_e \gtrsim 10^{11}$ cm^{-3}, and Si III λ1892 at $>10^{11}$ cm^{-3}. These lines can then be used to give additional constraints on the emission measure distribution and are included in Figure 5.

The C III λ1909 line provides the most sensitive limit on N_e at low densities. The ratio of C III λ1909 to Si III λ1892 is particularly useful because of the close proximity of these lines in wavelength. The variation of the ratio with N_e has been calculated by Cook and Nicolas (1979). We have recalculated their curve using the new atomic data for Si III and adopting the abundances given in Table 3, rather than those of Ross and Aller (1976) used by Cook and Nicolas. The observed ratio then agrees with that calculated in the low density limit to within $\pm 25\%$. This limits the density to $N_e \leq 2 \times 10^9 \pm 2 \times 10^9$ cm^{-3}, corresponding to P_e (at 5.6×10^4 K) $\leq 1.1 \times 10^{14}$ cm^{-3} K.[5]

Further confirmation of the density comes from plotting the C III λ1909 emission measure loci for $N_e = 10^9$ and 10^{10} cm^{-3}. Comparison with density insensitive loci in the same temperature range indicates $N_e < 10^{10}$ cm^{-3}.

We adopt an electron pressure of 1.1×10^{14} cm^{-3} K as a "typical" value for our "optimum" model, discussed in § V, although we also consider lower and higher pressures.

Basri, Linsky, and Eriksson (1981) found a discrepancy of over an order of magnitude between the electron pressure near the top of their chromospheric model and that implied by density-sensitive transition region lines. This discrepancy has been greatly reduced by adopting more recent atomic data and abundances measured for β Dra. Further comparisons with the model by Basti *et al.* are made below.

An additional method can be used to place approximate limits on the electron density. This relies on the ratio of the flux and opacity which are proportional to $\int N_e^2 dh$ and $\int N_e dh$, respectively (see Jordan and Brown 1981). Provided the total line width ($\Delta\lambda$, FWHM) is used, the effective opacity at line center, τ_0, can be related to the line surface flux of a collisionally excited line by

$$\frac{\tau_0}{F_*} = \frac{6.1 \times 10^{-6} \lambda^2(\text{Å}) T_e^{3/2} \exp(W_{12}/kT_e)}{\bar{g} P_e \Delta\lambda(\text{Å})}, \qquad (3)$$

where $\bar{g}$ is the Gaunt factor, taken from Burton *et al.* (1971). A Doppler-broadened line is assumed, which is obviously an approximation. In the discussion above it was shown that the resonance lines of C II, Si IV, and C IV are all expected to have $\tau_0 \gtrsim 1$ because of their widths, but those of N V have similar widths to the intersystem lines and should be optically thin. Here, we use these constraints to place limits on P_e. The upper and lower limits on P_e thus derived are given in Table 4. If C II is formed at 3×10^4 K, the mean of the stronger component of each multiplet gives $9 \times 10^{13} > P_e > 4 \times 10^{13}$ cm^{-3} K. Since equation (3) is a very simple approximation, this pressure range is not significantly different from the upper limit of $\sim 1.1 \times 10^{14}$ cm^{-3} K found from line ratios. However, any concentration of the emission to some fraction of the surface area could easily remove a small discrepancy between the pressures derived from line ratios and equation (3). Conversely, the absence of a large discrepancy in the sense of line ratios giving a higher value than the opacity argument suggests that density inhomogeneities have little effect on the transition region lines.

We conclude that at 5.6×10^4 K the electron pressure lies in the range $1.1 \times 10^{14} > P_e > 4 \times 10^{13}$ cm^{-3} K, and in the fol-

[5] In this paper we use the term electron pressure to refer to $P_e = N_e T$ and the term pressure to refer to $P = N_{\text{total}} T$.

TABLE 4

PRESSURE ESTIMATES FROM τ_0/F_*

Ion	λ (Å)	log T_m (K)	τ_0	P_e (cm^{-3} K)
N V	1239	5.2	≤1	≥4.2(13)
	1243	...	...	≥2.9(13)
C IV	1548	5.0	≥1	≤8.7(13)
	1551	...	...	≤5.0(13)
Si IV	1394	4.85	≥1	≤5.9(13)
	1403	...	...	≤3.4(13)
C II	1336	4.3	≥1	≤3.1(14)
		4.5	...	≤8.7(13)
		4.6	...	≤5.8(13)

lowing section we construct models to include this range. Pressures in this range indicate that the time scales for the atomic collision and radiative process are short, allowing the application of emission measure analysis to the spectra of β Dra.

V. ATMOSPHERIC STRUCTURE

a) Methods

The mean emission measure distribution determined in § IV may be used to calculate models of the chromosphere, transition region, and corona using the methods developed in earlier solar and stellar work (e.g., Jordan and Wilson 1971; Brown and Jordan 1981). At $T_e \geq 2 \times 10^4$ K, where hydrogen is predominantly ionized, $N_H \approx 0.8 N_e$, and the emission measure can be rearranged to give the temperature gradient for an assumed plane-parallel atmosphere,

$$dT_e/dh = P_e^2/[2.0E_m(T_e)T_e] \, . \quad (4)$$

Here we assume $E_m(T_e) = 0.7E_m(0.3)$, where $E_m(0.3)$ indicates the average over $\Delta \log T_e = 0.3$. The pressure, expressed in terms of P_e, is assumed to vary in hydrostatic equilibrium, giving

$$dP_e/dh = -7.14 \times 10^{-9} P_e g_*/T_e \, , \quad (5)$$

where g_*, the stellar surface gravity, is 40 cm s^{-2} (Luck 1982). Models of the pressure variation are calculated by combining equations (4) and (5) to give

$$P_e^2 = P_0^2 + 2.8 \times 10^{-8} g_* \int_{T_e}^{T_0} E_m(T_e) dT_e \, , \quad (6)$$

where P_0 and T_0 refer to the electron pressure and temperature at the top of the model, which in this case corresponds to log $T = 5.3$, just above the region where N V is formed. The assumption of hydrostatic equilibrium is required in making these models since there are insufficient independent measurements of N_e.

b) Spherically Symmetric Models

Models have been calculated with the following electron pressures at 2.5×10^5 K; $P_0 = 7.0 \times 10^{14}$, 3.5×10^{14}, 1.1×10^{14}, 5.0×10^{13}, and 0 cm^{-3} K, the final value corresponding to the minimum pressure model when each layer has its hydrostatic isothermal scale height. Equation (6) is used with the mean emission measure distribution to find the variation of electron pressure with temperature. The temperature gradients and temperature versus height are then found from equation (4). The resulting models of temperature versus height are shown in Figure 6. Because the gravity is low, the second term in equation (6) contributes little until below $\sim 10^4$ K. Models with $P_e \gtrsim 5.0 \times 10^{13}$ cm^{-3} K, therefore, have almost constant pressure between 2×10^5 and 2×10^4 K. However, models with $P_e \lesssim 1.6 \times 10^{13}$ cm^{-3} K are dominated by the second term in equation (6).

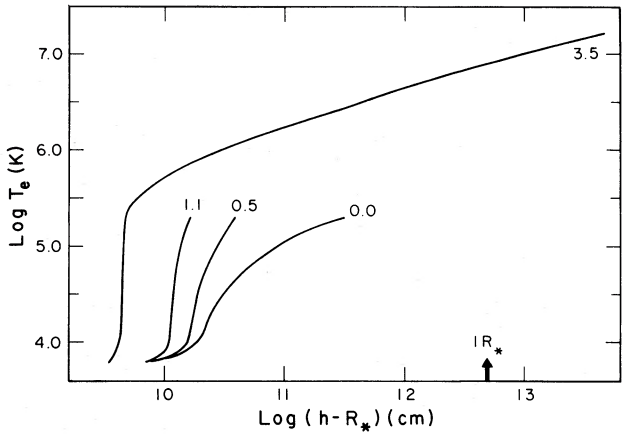

FIG. 6.—Variation of temperature with height for the computed models of the outer atmosphere of β Dra. The different models are identified by the value of the electron pressure at 2×10^5 K (P_0) which has units of 10^{14} cm^{-3} K. The model with $P_0 = 3.5 \times 10^{14}$ cm^{-3} K is extended to coronal temperatures using the method described in the text. The other models cannot be extended above 2×10^5 K without assuming that the X-ray emitting plasma in the corona is geometrically confined.

Another way of comparing the models for different assumed values of P_0 is to plot N_e (or $[N_e N_H]^{1/2}$, if including regions below 2×10^4 K) against T_e. These models are plotted in Figure 7, together with values of N_e previously derived from line ratios or opacity arguments, including a range of values for C II depending on T_e (see Table 4). Also illustrated is the model by Basri, Linsky, and Eriksson (1981), which was calculated primarily from the Mg II and Ca II resonance lines with only a simple assumed structure for the transition region above. Basri *et al.* do not claim any great accuracy for their model above

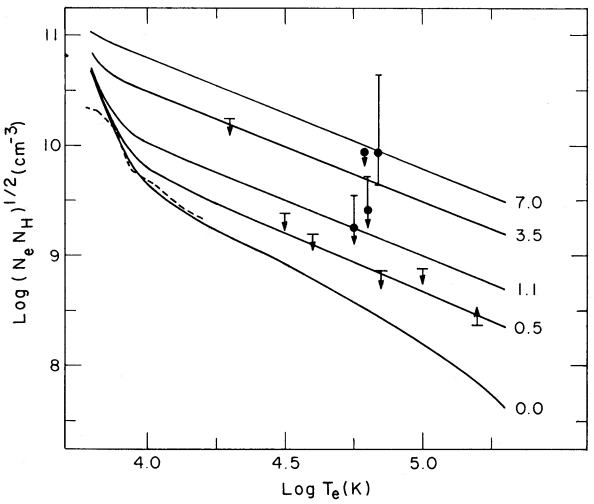

FIG. 7.—Variation of $(N_e N_H)^{1/2}$ with temperature for a selection of models with electron pressure, P_0, at 2×10^5, indicated in units of 10^{14} cm^{-3} K. Pressure estimates obtained from emission-line ratios are shown as filled circles with appropriate error bars. Pressure limits from line opacity arguments are also shown. The model of Basri *et al.* (1981) is shown as a dashed line.

8000 K. Although some disagreement remains, the model by Basri *et al.* does not give significantly lower transition region pressures than those we calculate for $P_0 < 1.1 \times 10^{14}$ cm^{-3} K. The zero top pressure ($T_{\rm corona} \approx 2 \times 10^5$ K) model would be required to achieve agreement in the transition region. Use of the alternative mean emission measure distribution, shown in Figure 5, does not significantly alter the models shown in Figure 7. The main change is an increase in $(N_e N_{\rm H})^{1/2}$ below 10^4 of $\sim 4\%$.

Figure 7 shows that at $T_e \lesssim 10^4$ K all the realistic models tend to the same value of $(N_e N_{\rm H})^{1/2}$, because the second term of equation (6) dominates. In a hydrostatic atmosphere this would imply that the low temperatures lines are formed over an isothermal hydrostatic scale height, enabling $(N_e N_{\rm H})^{1/2}$ to be found from, for example, the Mg II flux if the surface gravity is known. However, in practice, the nonthermal motions will extend the atmosphere and should also be taken into account. If this behavior is generally true, the Mg II flux should scale as $N_e N_{\rm H}/g_{\rm eff}$, where $g_{\rm eff}$ is the "effective" gravity. This is a more complex scaling law than hitherto considered (e.g., McClintock *et al.* 1975; Kelch *et al.* 1978).

Since the nonthermal motions do not correspond to turbulent pressures greatly in excess of the gas pressure and there is a comparable uncertainty in the gas pressure, models including turbulent support are not presented. Including a turbulent pressure a factor of 3 larger than the gas pressure would be equivalent to decreasing the second term of equation (6) by the same factor. Since the first term dominates at $T_e \geq 2 \times 10^4$ K in all but models close to the low pressure limit model, the effect of the turbulent support is negligible for P_0 (at 2×10^5 K) $\gtrsim 1.6 \times 10^{13}$ cm^{-3} K.

c) *The X-Ray Fluxes and Structure above 2 × 10^5 K*

The X-ray flux of 7.2×10^{-12} ergs cm^{-2} s^{-1} measured with the *Einstein Observatory* imaging proportional counter (IPC) (Ayres *et al.* 1981) can be converted to a stellar flux by assuming an inner radius, R_x, for the X-ray emitting region, which we take to be a shell of thickness H. Applying the emissivities of Tucker and Koren (1971), folded with the IPC pass band leads to an emission measure that depends on the temperature of the emitting region. Expressing this emission measure, $E_m(h)$, in terms of the stellar surface flux gives

$$E_m(h) = 5.7 \times 10^{27} \frac{T_e}{10^7} \left(\frac{R_*}{R_x}\right)^2 . \quad (7)$$

The emission measure can also be written as

$$E_m(h) \approx \overline{N_e^2} H . \quad (8)$$

If the X-ray emission is formed in an isothermal corona, H is the hydrostatic isothermal scale height,

$$H = 3.6 \times 10^6 T_e \frac{g_*}{g_x} = 3.6 \times 10^6 T_e \left(\frac{R_x}{R_*}\right)^2 , \quad (9)$$

where g_x and R_x refer to the height of the X-ray emission.

The mean (rms) electron density can then be found from relations (7) and (9); i.e.,

$$(\overline{N_e^2})^{1/2} = 1.26 \times 10^7 \left(\frac{R_*}{R_x}\right)^2 . \quad (10)$$

Because the emission measure distribution is not known between 2×10^5 and 1.5×10^7 K, it is not possible to use equation (6) to make a self-consistent model of the variation of the P_e and T_e with height. However, an upper limit to the coronal electron density can be found by taking $R_* = R_x$. This gives

$$(\overline{N_e^2})^{1/2} \leq 1.3 \times 10^7 \text{ cm}^{-3} . \quad (11)$$

We have adopted a stellar radius of 4.9×10^{12} cm (70 $R_\odot$) based on a distance to the star of 200 pc. This distance is implied by the absolute magnitude of ~ -4.0 appropriate to a luminosity class Ib–II star. A smaller distance, as implied for instance by the star's very uncertain parallax, seems unlikely given the strength of the interstellar absorption seen in the stellar H Lyα line. If the X-ray region is treated as a simple extension of that at 10^5 K, then the electron pressure of $\sim 10^{14}$ cm^{-3} K at 10^5 K suggests a coronal temperature $T_c \geq 8 \times 10^6$ K. The temperature measured with the IPC is 1.5×10^7 K (G. Vaiana, private communication), consistent with the above lower limits. Using $T_c = 1.5 \times 10^7$ K, the upper limit to the coronal pressure is 1.9×10^{14} cm^{-3} K.

Since $R_x > R_*$ and $H \geq 5.4 \times 10^{13}$ cm, it is clear that the X-ray emission measure, $E_m(T)$, shown in Figure 5 is an upper limit. For illustrative purposes only a model connecting the EUV and X-ray emitting region has been made by adopting a linear interpolation between 2×10^5 and 1.5×10^7 K, such that $d \log E_m / d \log T = 0.4$. With $R = R_*$ and $g = g_*$ (eventually a variable R and g should be introduced) and the pressure variation given by equation (6), a base pressure (at 2×10^5 K) of 3.5×10^{14} cm^{-3} K is found. This model is shown in Figure 6. More realistic models would be even more extended.

It can be seen from Figure 5 that the gradient of the linear interpolation is less than the value of 3/2 commonly found in the solar atmosphere (Jordan 1980). This implies that thermal conduction deposits energy in each layer below the corona. In the Sun this situation is not compatible with a static solution since the energy cannot be radiated away locally, but in β Dra where the emission measures are larger and the gravity lower, the radiation losses are larger, while the temperature gradients and conductive fluxes are smaller (see § VI also). Thus, the linear fit ($d \log E_m / d \log T = 0.4$) used for β Dra is compatible with a static solution.

Confining the X-ray emission geometrically would result in a higher value of the "coronal" pressure, which would then be even more inconsistent with the pressure measured spectroscopically in the transition region. The only type of solution admissible would then be one in which the contribution from high pressure regions in the transition region is, because of a limited area coverage, negligible compared with the average contribution, although it is only from these confined regions that X-rays are emitted. Such a model is consistent with how active regions affect the integrated spectrum of the solar atmosphere. In such a model it would not be correct to simply interpolate the emission measure between the region at 2×10^5 and 1.5×10^7 K.

In the absence of closed magnetic fields, the escape velocity at the stellar surface (or the temperature of the critical point of a thermally driven wind) would limit the coronal temperature to $T_{\rm esc} \leq 1 \times 10^6$ K, far less than indicated by the X-ray data. Taking $R_x \approx 2\ R_*$ (a lower limit suggested by the $P_0 = 3.5 \times 10^{14}$ model in Fig. 7) would give $T_{\rm esc} \approx 7.7 \times 10^5$ K. It is clear, therefore, that the X-ray emission cannot originate in a thermally driven (solar-like) wind. Either the emission comes from regions confined by a magnetic field (perhaps analogous

to solar coronal loops), or if not confined, then from an expanding plasma heated by some unknown process which is capable of heating the plasma to 20 times T_{esc}. However, the transition region lines (i.e., the relative wavelengths of the optically thin lines) do not indicate the presence of a wind. Further X-ray and EUV observations are required to investigate the emission measure distribution between $\sim 2 \times 10^5$ and 10^7 K.

VI. ENERGY BALANCE

One of the major questions concerning the physics of stellar chromospheres and coronae is what energy transport and deposition processes give rise to the observed phenomena. Although the energy must originate in subphotospheric convection zones, even in the Sun no satisfactory mode of energy transport or deposition has been found. Further information may be obtained from the study of the behavior in a range of stars with differing photospheric properties.

The energy flux into the chromosphere and transition region, F_m, must be balanced by the radiative, conductive, and wind losses; i.e., for any local region of the atmosphere the net input flux, ΔF_m, must balance the net local energy transfer

$$\Delta F_m = \Delta F_R + \Delta F_c + \Delta F_f \,. \tag{12}$$

The radiative loss is closely related to the observed fluxes since

$$\Delta F_R \approx 0.8 E_m P_{\rm rad} \,, \tag{13}$$

for $T_e \gtrsim 10^4$ K and ΔF_R is summed over $\Delta \log T = \pm 0.15$. The quantity $P_{\rm rad}$ is the power loss function, and we have used the values of McWhirter, Thoneman, and Wilson (1975). Thermal conduction transports energy down from the corona, and the conductive flux is given by

$$F_c \approx -10^{-6} T_e^{5/2} \frac{dT_e}{dh} \,. \tag{14}$$

The net conductive flux, ΔF_c, may either deposit energy in or transport energy out of a given region. The energy flux in a flow consists of kinetic energy, enthalpy flux, and potential energy; i.e.,

$$F_f = \frac{1}{2} \rho v^3 + 5\rho \frac{k}{M_{\rm H}} Tv + \rho g_* R v \,, \tag{15}$$

where v and ρ are the flow velocity and density and R is the radial distance. However, since we have no evidence for a stellar wind in the region where the observed far-UV emission lines are formed, the wind energy term is taken to be zero. Because densities are low, quite large velocities are required before the wind energy becomes comparable with the radiative losses.

The terms of the energy balance in the spherically symmetric model with a top electron pressure, $P_0 = 1.1 \times 10^{14}$ cm^{-3} K, are given in Table 5 summed over intervals of 0.1 dex. Unless the pressure becomes very high, thermal conduction is negligible compared with the observed radiative losses. The total radiative loss between 10^4 and 1.5×10^5 K is $\sim 1.5 \times 10^7$ ergs cm^{-2} s^{-1}, which is ~ 60 times the equivalent quiet-Sun value, and slightly larger than the losses in the low chromosphere lines of Ca II and Mg II (Basri and Linsky 1979). Use of the alternative mean emission measure distribution shown in Figure 5 would increase the total radiative losses by a factor of 3. Most of this radiation would be emitted in the H Lyman lines, which at present are not directly measurable.

TABLE 5

TERMS OF THE ENERGY BALANCE[a]

log T_e (K)	log E_m (cm^{-5})	ΔF_R (ergs cm^{-2} s^{-1})	ΔF_c (ergs cm^{-2} s^{-1})	F_m (ergs cm^{-2} s^{-1})
3.9.....	30.75	2.9(6)	...	1.8(7)
4.0.....	29.75	3.2(6)	...	1.5(7)
4.1.....	28.95	2.9(6)	...	1.2(7)
4.2.....	28.55	2.6(6)	...	8.5(6)
4.3.....	28.40	1.5(6)	...	5.9(6)
4.4.....	28.30	7.8(5)	...	4.4(6)
4.5.....	28.18	5.0(5)	...	3.6(6)
4.6.....	28.10	4.5(5)	...	3.1(6)
4.7.....	27.98	5.4(5)	...	2.6(6)
4.8.....	27.80	6.6(5)	−1.7(2)	2.1(6)
4.9.....	27.63	5.5(5)	−2.9(2)	1.4(6)
5.0.....	27.50	4.1(5)	−6.3(2)	8.9(5)
5.1.....	27.34	2.7(5)	−9.0(2)	4.9(5)
5.2.....	27.25	2.2(5)	−8.6(2)	2.2(5)

[a] $P_0 = 1.1 \times 10^{14}$ cm^{-3} K.

The energy input required to account for the radiative losses can be compared with the energy which could be carried by various types of wave. If the observed emission-line widths are assumed to be predominantly due to the passage of plane waves through the stellar outer atmosphere, the energy carried by these waves can be estimated. The "nonthermal" most probable speed, ξ_0, is related to the observed line widths and thermal widths by

$$\xi_0^2 = 3.3 \times 10^{20} \left(\frac{\Delta\lambda}{\lambda} \right)^2 - 1.66 \times 10^8 \frac{T_e}{m_i} \,, \tag{16}$$

where $\Delta\lambda$ is the measured FWHM and m_i is the ion mass relative to the proton mass. If the nonthermal motions are isotropic, the rms value of ξ_0 is

$$\langle V_T^2 \rangle = \tfrac{3}{2} \xi_0^2 \,. \tag{17}$$

The nonthermal energy density can then be combined with the speeds expected from, for instance, sound waves, C_s, and Alfvén waves, C_A, in order to find the energy flux. For plane waves these speeds are given (for $T_e \gtrsim 2 \times 10^4$ K) by

$$C_s = (\gamma P/\rho)^{1/2} \approx 1.46 \times 10^4 T_e^{1/2} \text{ cm s}^{-1} \,, \tag{18}$$

adopting the solar mean molecular weight with $\gamma = 5/3$, and

$$C_A = B/(4\pi\rho)^{1/2} \approx 2 \times 10^{11} B T_e^{1/2} P_e^{-1/2} \text{ cm s}^{-1} \,, \tag{19}$$

where B is the magnetic field strength and P and ρ are the gas pressure and density.

The derived values of ξ_0 and $\langle v_T^2 \rangle^{1/2}$ and the values calculated for C_s and C_A/B using our model with $P_0 = 1.1 \times 10^{14}$ cm^{-3} K are given in Table 6. It is assumed that the line broadening is due only to thermal broadening and the turbulent motions associated with the passage of waves. The velocities for C II, Si IV, and C IV are upper limits since the widths of these lines are dominated by opacity effects. Figure 8 compares the observed radiative losses with the upper limits to the deduced energy flux, derived from line widths assuming a wave speed equal to the sound speed. The energy fluxes derived from the optically thin lines agree reasonable well with the mechanical fluxes implied by the radiation losses. The optically thick lines are, of course, broader. The values of the energy flux derived from $\rho V_T^2 C_s$ are dependent on the densities in the model, but these could be brought into closer agreement with the radiation losses by a small increase in pressure.

TABLE 6

DEDUCED NONTHERMAL AND WAVE VELOCITIES

Ion	λ (Å)	$\Delta\lambda/\lambda$	T_e (K)	ξ_0 (km s^{-1})	$\langle v_T^2\rangle^{1/2}$ (km s^{-1})	C_s (km s^{-1})	C_A/B (km s^{-1} G^{-1})
S I	1295.7	2.5(−4)	6.3(3)	41	50	9	7
	1296.2	3.1(−4)	...	53	65	...	...
Si II	1808.0	3.3(−4)	2.0(4):	57	70	21	27
C II	1335.7	6.5(−4)	3.2(4)	117	143	26	34
Si III	1892.0	3.5(−4)	5.0(4)	61	74	33	42
C III	1908.7	2.9(−4)	5.6(4)	49	60	35	45
O III	1666.2	3.3(−4)	6.8(4)	56	69	38	49
Si IV	1393.6	5.2(−4)	7.1(4)	92	113	39	50
	1402.8	6.2(−4)	...	111	140	...	...
C IV	1548.2	5.2(−4)	1.0(5)	92	113	46	60
	1550.8	6.5(−4)	...	116	142	...	...
N V	1238.8	4.4(−4)	1.6(5)	77	95	58	76
	1242.8	4.2(−4)	...	74	91	...	...

The mode of energy transport cannot yet be uniquely identified. Clearly, pure acoustic waves (with $V_T = C_s$) cannot carry sufficient energy as shown in Figure 8. However, supersonic shock waves cannot be ruled out as the heating mechanism and would require Mach numbers of ~ 10, 5.5, and 3 at 10^4, 3×10^4, and 10^5 K, respectively.

If β Dra possesses a magnetic field as is likely given the coronal temperature and large surface fluxes, MHD waves may contribute to the energy deposition. From Table 6 and Figure 8 it can be seen that in the idealized case of pure Alfvén waves (with C_A as the propagation velocity) an average magnetic field strength of ~ 2 gauss would provide sufficient flux to account for F_m. This field strength does not seem unduly large when compared with the strength of fields seen in dwarfs stars such as the Sun.

In § III we concluded that the line profiles and relative wavelengths suggest circulation motions rather than a mass-conserving wind. Using the upper limit to the electron pressure of $P_e \lesssim 1.1 \times 10^{14}$ cm^{-3} and a relative velocity of 8 km s^{-1}, we find that both the kinetic energy flux and the enthalpy flux associated with these motions are negligible compared with the local radiation losses.

However, the radiation losses can be matched by the energy flux found by treating the nonthermal motions as an energy density propagating at the same nonthermal velocity. The relation between these motions and the energy source is not clear but could conceivably be the result of energy redistribution following heating by magnetic energy dissipation rather than wave energy dissipation.

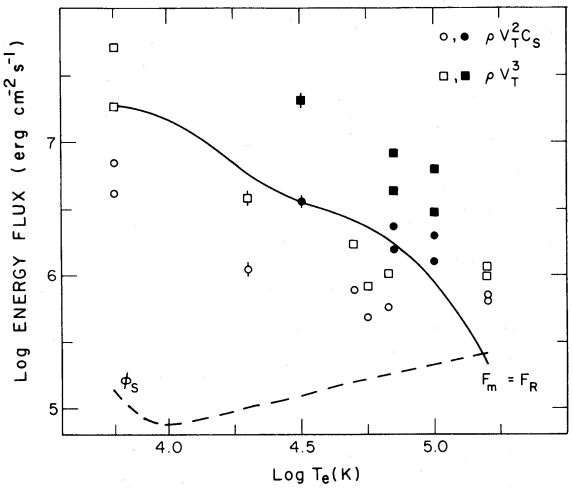

FIG. 8.—Energy input, F_m, required to account for the observed radiative losses as a function of temperature for the model with $P_0 = 1.1 \times 10^{14}$ cm^{-3} K. Dashed line shows the energy flux available from pure acoustic waves. Solid line is the energy flux input derived by summing the radiative losses in all higher temperatures parts of the model. Energy fluxes derived from the observed line widths, corrected for instrumental broadening, are shown for propagation velocities equal to the sound velocity (*circles*) and the turbulent velocity (*squares*). Optically thin lines are indicated by open symbols. Filled symbols indicate lines thought to be optically thick and hence subject to extra broadening. Typical error bars (1 σ) due to the measurement error in the line width are shown for Si II (1808 Å) and C II (1336 Å). Error bars for the C IV lines are smaller than the plotted symbols.

VII. CONCLUSIONS

We report here an analysis of the longest continuous *IUE* exposure, a 1273 minute high dispersion SWP spectrum of β Dra (G2 Ib–II), together with low dispersion spectra, obtained with the aim of understanding the atmospheric structure of this bright star located in a crucial region of the H-R diagram. Our conclusions are as follows:

1. The line widths and multiplet ratios of the C II, Si IV, and C IV resonance lines indicate that these lines are at least marginally optically thick. The redward asymmetries of these resonance lines can be explained by line formation in a turbulent medium with a combination of accelerating upflows and decelerating downflows. However, the intersystem lines formed at $T_e \approx 5$–7×10^4 K are displaced by $+8 \pm 4$ km s^{-1} and the optically thin lines of Si II, He II, and N V show similar redward displacements compared with neutral optically thin chromospheric lines chosen to define the zero velocity. It seems likely that the downflows implied by the observed redshifts are components of circulation motions in the stellar atmosphere as suggested by Basri, Linsky, and Eriksson (1981).

2. We have used our emission measure method for analyzing collisionally excited, effectively thin emission lines, which we modified to include new atomic data and the nonsolar abundances of β Dra. Except for the Si III λ1206 line, whose flux may be significantly underestimated, these lines result in a consistent emission measure distribution between 10^4 and 2×10^5 K.

3. The density-sensitive line ratios C III λ1909/O III λ1666, O III λ1666/Si IV λ1403, and C III λ1909/Si IV λ1403 indicate $N_e \lesssim 1 \times 10^{10}$ cm^{-3} at 5–7 $\times 10^4$ K. The C III λ1909 line is most sensitive to density at these low densities, and the C III

λ1909/Si III λ1892 ratio implies $N_e \leq 2 \times 10^9$ cm^{-3} and $P_e = N_e T_e \leq 1.1 \times 10^{14}$ cm^{-3} K. The ratios of line center optical depth to line surface flux for the C II, Si IV, C IV, and N V resonance lines place P_e in the range 4–9 $\times 10^{13}$ cm^{-3} K. This range of transition region electron pressure is about an order of magnitude smaller than for the quiet Sun, and is not significantly inconsistent with the value predicted by the Basri *et al.* chromospheric model for β Dra.

4. If the corona is not extended geometrically, then the observed soft X-ray flux obtained with the IPC on the *Einstein* satellite implies that in the corona $(\overline{N_e^2})^{1/2} \leq 1.3 \times 10^7$ cm^{-3}, and the observed temperature of the X-ray emitting plasma ($\sim 1.5 \times 10^7$ K) implies that its electron pressure is $\leq 1.9 \times 10^{14}$ cm^{-3} K. However, the coronal isothermal scale height is $\sim 10\ R_*$, implying that the coronal emission measure and pressure must be lower.

5. The escape temperature from the stellar surface is $\sim 1 \times 10^6$ K and even lower if the plasma is in an extended corona. Since the temperature of the X-ray emitting plasma is much larger, either this hot plasma is confined by a magnetic field, or if not, then it is heated by some process which is capable of heating plasma to $20 \times T_{esc}$. The X-ray emission cannot originate in a thermally driven wind, and there is no evidence for a wind in either the X-ray or ultraviolet data. Overall the most satisfactory model is one where the average atmosphere has a coronal temperature less than 1×10^6 K in which small regions of confined hot material exist.

6. We find that thermal conduction and wind expansion, if any, are negligible compared to radiative losses in the transition region and coronal energy balance. We consider whether various types of waves can account for the necessary energy input by estimating the nonthermal motions from the observed line widths. Pure acoustic waves cannot carry sufficient energy, but MHD waves could explain the energy input to the upper chromosphere and transition region.

A number of observations could be made in the future to further investigate the structure and energy balance of the outer atmosphere of β Dra. The greater sensitivity and spectral resolution of the Space Telescope could be used to improve the line profiles and measurements of relative motion. EUV and further X-ray observations should be able to fill in the gap in the emission measure distribution between 2×10^5 K and 1.5×10^7 K. Free-free radio emission from any high temperature outflow around the star may be detected with the VLA telescope.

Notes added in manuscript (1984 April 9).—C. Mendoza (*J. Phys. B*, **14**, 2465 [1981]) has calculated the averaged collision strength for the Mg II resonance doublet to be 16.5 (at 10^4 K), and this value is more appropriate than the value of 35.4 used in this paper. Use of this value affects only the coolest part of our emission measure distribution where our methods are, in any case, least applicable. Use of the amended emission measure distribution leads to larger pressures in the lower part of our models (e.g., increases of 12% and 55% at 10^4 K in the $P_0 = 1.1 \times 10^{14}$ and 0 cm^{-3} K models). This would tend to increase any discrepancy between our models and that of Basri, Linsky, and Eriksson (1981). Larger transition region heights result (e.g., 2.8×10^{10} cm rather than 1.3×10^{10} cm for the 1.1×10^{14} cm^{-3} K model), and the total mechanical flux required increases by a factor of 2 with the additional deposition confined to the lower part of the models. The bulk of our paper and our conclusions are not significantly altered by this change.

S. A. Drake and A. Brown have observed β Dra with the VLA radio telescope at 6 cm in 1983 July. The derived 3 σ upper limit was 0.35 mJy. This implies an ionized mass-loss rate of less than $1.8 \times 10^{-8}\ M_\odot$ yr^{-1} for an assumed wind velocity of 100 km s^{-1}. The mass-loss rate is directly proportional to the wind velocity.

We would like to thank the staff at the NASA GSFC and ESA VILSPA *IUE* ground stations for their assistance in obtaining these observations and Dr. E. Brugel and his colleagues at the *IUE* Regional Data Analysis Facility in Boulder, supported by grant NASA5-26409, for their help with data reduction. This work was supported in part by NASA grants NAG5-82, NGL-06-003-057 and NAG5-199 through the University of Colorado and also by the United Kingdom Science and Engineering Research Council.

REFERENCES

Ake, T. B. 1981, *IUE Newsl.*, No. 15, p. 60.
Athay, R. G. 1972, *Radiation Transport in Spectral Lines* (Dordrecht: Reidel).
Ayres, T. R., Linsky, J. L., Basri, G. S., Landman, W., Henry, R. C., Moos, H. W., and Stencel, R. E. 1982, *Ap. J.*, **256**, 550.
Ayres, T. R., Linsky, J. L., Vaiana, G. S., Golub, L., and Rosner, R. 1981, *Ap. J.*, **205**, 293.
Ayres, T. R., Stencel, R. E., Linsky, J. L., Simon, T., Jordan, C., Brown, A., and Engvold, O. 1983, *Ap. J.*, **274**, 801.
Baliunas, S. L., and Butler, S. E. 1980, *Ap. J. (Letters)*, **235**, L45.
Baluja, K. L., Burke, P. G., and Kingston, A. E. 1980*a*, *J. Phys. B*, **13**, L543.
———. 1980*b*, *J. Phys. B*, **13**, 829.
———. 1981, *J. Phys. B*, **14**, 1333.
Barnes, T. G., Evans, D. S., and Moffett, T. J. 1978, *M.N.R.A.S.*, **183**, 285.
Basri, G. S. 1980, *Ap. J.*, **242**, 1133.
Basri, G. S., and Linsky, J. L. 1979, *Ap. J.*, **234**, 1023.
Basri, G. S., Linsky, J. L., and Eriksson, K. 1981, *Ap. J.*, **251**, 162.
Bohlin, R. C., and Holm, A. V. 1981, *ESA IUE Newsl.*, No. 11, p. 18.
Breakiron, L. A., and Upgren, A. R. 1979, *Ap. J. Suppl.*, **41**, 709.
Brown, A., and Jordan, C. 1980, *M.N.R.A.S.*, **191**, 37p.
———. 1981, *M.N.R.A.S.*, **196**, 757.
Brown, A., Jordan, C., Ayres, T. R., Linsky, J. L., and Stencel, R. E. 1982, in *Proc. 3d European IUE Conf.* (ESA-SP176), p. 161.
Brueckner, G. E. 1981, in *Solar Active Regions*, ed. F. Q. Orrall (Boulder: Colorado Associated University Press), p. 113.
Burton, W. M., Jordan, C., Ridgeley, A., and Wilson, R. 1971, *Phil. Trans. Roy. Soc. London, A*, **270**, 81.
Cassatella, A., Ponz, D., and Selvelli, R. L. 1981, *NASA IUE Newsl.*, No. 14, p. 270.
Cook, J. W., and Nicolas, K. R. 1979, *Ap. J.*, **229**, 1163.
Cowan, R. D., Hobbs, L. M., and York, D. G. 1982, *Ap. J.*, **257**, 373.
Dere, K. P. 1982, *Solar Phys.*, **77**, 77.
Doschek, G. A., Feldman, U., Bhatia, A. K., and Mason, H. E. 1978, *Ap. J.*, **226**, 1129.
Doschek, G. A., Feldman, U., and Bohlin, J. D. 1976, *Ap. J. (Letters)*, **205**, L177.
Dufton, P. L., Berrington, K. A., Burke, P. G., and Kingston, A. E. 1978, *Astr. Ap.*, **62**, 111.
Dupree, A. K. 1981, in *Advances in Ultraviolet Astronomy*, ed. Y. Kondo, J. M. Mead, and R. D. Chapman (NASA CP2238), p. 3.
Dupree, A. K., Foukal, P. V., and Jordan, C. 1976, *Ap. J.*, **209**, 621.
Feldman, U., Cohen, L., and Doschek, G. A. 1982, *Ap. J.*, **255**, 325.
Gabriel, A. H., and Jordan, C. 1972, in *Case Studies in Atomic Collision Physics 2*, ed. E. W. McDaniel and M. R. C. McDowell (Amsterdam: North-Holland), p. 209.
Hartmann, L., Dupree, A. K., and Raymond, J. C. 1980, *Ap. J. (Letters)*, **236**, L143.
———. 1981, *Ap. J.*, **246**, 193.
Hayes, M. A. 1982, *M.N.R.A.S.*, **200**, 49p.
Hummer, D. G., and Rybicki, G. S. 1968, *Ap. J. (Letters)*, **153**, L107.
Jackson, A. R. G. 1973, *M.N.R.A.S.*, **165**, 53.
Jordan, C. 1965, Ph.D. thesis, University of London.
———. 1969*a*, *M.N.R.A.S.*, **142**, 501.
———. 1969*b*, *Ap. J.*, **156**, 49.
———. 1980, *Astr. Ap.*, **86**, 355.
Jordan, C., and Brown, A. 1981, in *Solar Phenomena in Stars and Stellar Systems*, ed. R. M. Bonnet and A. K. Dupree (Dordrecht: Reidel), p. 199.

Jordan, C., Brueckner, G. E., Bartoe, J.-D. F., Sandlin, G. D., and Van Hoosier, M. E. 1978, *Ap. J.*, **226**, 687.
Jordan, C., and Wilson, R. 1971, in *Physics of the Solar Corona*, ed. C. J. Macris (Dordrecht: Reidel), p. 211.
Kelch, W. L., Linsky, J. L., Basri, G. S., Chiu, H.-Y., Chang, S.-H., Maran, S. P., and Furenlid, I. 1978, *Ap. J.*, **220**, 962.
Kelly, R. L., and Palumbo, L. J. 1973, *Atomic and Ionic Emission Lines below 2000 Angstroms* (NRL Rept. No. 7599).
Kingston, A. E., Thompson, A., Berrington, K. A., and Dufton, P. L. 1983, *J. Phys. B*, **16**, L207.
Laughlin, C., and Victor, G. A. 1979, *Ap. J.*, **234**, 407.
Linsky, J. L. 1981, in *Advances in Ultraviolet Astronomy*, ed. Y. Kondo, J. M. Mead, and R. D. Chapman (NASA CP2238), p. 17.
Linsky, J. L., and Haisch, B. M. 1979, *Ap. J. (Letters)*, **229**, L27.
Luck, R. E. 1977, *Ap. J.*, **218**, 752.
———. 1978, *Ap. J.*, **219**, 148.
———. 1982, *Ap. J.*, **256**, 177.
Luck, R. E., and Lambert, D. L. 1981, *Ap. J.*, **245**, 1018.
Magee, N. H., Mann, J. B., Merts, A. L., and Robb, W. D. 1977, Los Alamos Rept., No. LA-6691-MS.
McClintock, W., Linsky, J. L., Henry, R. C., Moos, H. W., and Gerola, H. 1975, *Ap. J.*, **202**, 165.
McWhirter, R. W. P., Thoneman, P. C., and Wilson, R. 1975, *Astr. Ap.*, **40**, 63.
Nicolas, K. R. 1977, Ph.D. thesis, University of Maryland.
Nussbaumer, H., and Storey, P. J. 1979, *Astr. Ap.*, **71**, L5.
Parkinson, W. H., Kwong, H. S., Smith, P. L., and Johnson, C. 1983, in *IAU Colloquium 73, Proc. 7th International Colloquium on Ultraviolet and X-Ray Spectroscopy of Astrophysical Plasmas*, in press.
Pottasch, S. R. 1964, *Space Sci. Rev.*, **3**, 816.
Roussel-Dupré, D., and Shine, R. A. 1982, *Solar Phys.*, **77**, 329.
Ross, J. E., and Aller, L. H. 1976, *Science*, **191**, 1223.
Savage, B. D., and Mathis, J. S. 1979, *Ann. Rev. Astr. Ap.*, **17**, 73.
Seaton, M. J. 1962, *Proc. Phys. Soc. London*, **79**, 1105.
Seely, J. F., and Feldman, U. 1984, *Ap. J.*, submitted.
Shine, R. A. 1983, *Ap. J.*, **266**, 882.
Stencel, R. E., and Mullan, D. 1980, *Ap. J.*, **240**, 718.
Tucker, W. H., and Koren, M. 1971, *Ap. J.*, **168**, 283.
Turnrose, B. E., and Harvel, C. A. 1982, *NASA IUE Newsl.*, No. 16, p. 1.
Underhill, A. B. 1981, *Astr. Ap.*, **97**, L9.
Withbroe, G. L. 1976, *Solar Phys.*, **45**, 301.

T. R. AYRES: Laboratory for Atmospheric and Space Physics, University of Colorado, Boulder, CO 80309

A. BROWN and J. L. LINSKY: Joint Institute for Laboratory Astrophysics, University of Colorado, Boulder, CO 80309

C. JORDAN: Department of Theoretical Physics, Oxford University, Oxford, England, UK

R. E. STENCEL: EZ-7, NASA Headquarters, Washington, DC 20546